Fast Imaging and Scattering Center Model Extraction with Full-Wave Computational Electromagnetics Formulations

Rainer Bunger*

Abstract—The so-called "fast imaging and scattering centers approach" originally proposed by Bhalla & Ling has revolutionized the generation of inverse synthetic aperture radar (ISAR) images and scattering center models using computational electromagnetics. Until now this approach has been used exclusively with ray-based methods. The main contribution of this paper is an extension of the Bhalla & Ling formulation for the generation of ISAR images and scattering center models with full-wave methods. Moreover, we discuss an approach to reduce the sampling requirements of the original Bhalla & Ling formulation, rendering the formulation applicable to 3-D imaging of real targets.

1. INTRODUCTION

ISAR images allow to visually identify different contributors to radar cross section (RCS). Since k-space (the RCS) and image space are related via Fourier transforms, the ISAR image contains the RCS information for all considered aspect angles and frequencies. This allows to evaluate camouflage concepts by k-space masking. Due to sampling requirements, image generation via discrete Fourier transform of the sampled RCS is extremely costly, even when using fast optic-asymptotic methods like the shooting and bouncing rays (SBR) method. The fast ISAR imaging and scattering center formulation for the SBR proposed by Bhalla & Ling [1–4] is based on the idea to analytically perform small angle and small bandwidth bistatic imaging integrals on a ray by ray basis, thus avoiding the dense RCS sampling requirements of the traditional algorithm.

The tight connection of Bhalla & Lings fast imaging and scattering centers algorithm to the SBR method is reasoned by the analytically known RCS contributions of the rays. This allows to perform bistatic imaging integrals analytically. It turns out that a necessary small angle and small bandwidth assumption is not a limitation in practice: Extracted scattering center models provide bandwidths of at least 20%, and the small angle assumption is overlaid by the small angle restriction of the bistatic to monostatic approximation [5]. An advantage of multiple bistatic images and scattering center models over a full-spherical monostatic image is that scattering centers could be easily assigned to the different directions of incidence.

A limitation of the published algorithm is that it relies on the so-called "Sullivan approach", which is essentially a fast 3-D convolution combined with an inverse interpolation ("anterpolation") onto grid points. Here a carrier phase exponential causes large interpolation errors which must be compensated by a dense mesh. The related workload is so large that it is generally advised to generate multiple 2-D images instead of a full 3-D image. We have modified the algorithm so that the anterpolation is free from the carrier exponential. The same idea has recently been published and described in greater detail by Yun et al. [6], but RCS computation is not covered there.

Another restriction of the Bhalla & Ling formulation is that it is combined with SBR. We will describe an extension of the formulation which allows to generate ISAR images and scattering center

models with full-wave methods like the multilevel fast multipole method (MLFMM), finite difference time domain technique (FDTD), and discontinuous Galerkin finite element method (DG-FEM).

To our knowledge the contribution published recently by Yun et al. is the first essential improvement of the Bhalla & Ling formulation which is also reflected by our quite short list of references.

The paper is organized as follows: In the following section we will describe how the Bhalla & Ling formulation is extended for full-wave methods. We will also indicate how the scattering center model could be used in time domain (but a corresponding application will not be shown). Section 3 will demonstrate that the derived scattering center models are indeed able to represent the RCS within the considered frequency band and bistatic angular range. We will not show ISAR images because the scattering center models derived from the ISAR images will give a better insight, especially in 3-D.

2. THEORY

2.1. Fast Image Generation

ISAR imaging approaches are based on the Fourier relation between the scattered farfield (the RCS) and the image. Bhalla & Ling [1] derive the concept for a perfectly conducting target under plane wave incidence (the derivation can also be found in [7, p125]). Furthermore, physical optics (PO) conditions are assumed. The scattered field $\vec{E}^{\mathrm{s}}$ is evaluated as a surface integral over the PO current densities. The introduction of an "object shape function" $O(\vec{r})$ allows to write the surface integral as a three-dimensional inverse Fourier transform:

$$\hat{p} \cdot \vec{E}^{\mathrm{s}}(\vec{r}) = C\tilde{O}\left(\vec{k}^{\mathrm{s}} - \vec{k}^{\mathrm{i}}\right) = C\mathcal{F}^{-1}\left\{O(\vec{r})\right\}\left(\vec{k}^{\mathrm{s}} - \vec{k}^{\mathrm{i}}\right) \tag{1a}$$

with the normalization constant

$$C = -jkE_0\frac{e^{-jkr}}{4\pi r}. \tag{1b}$$

In these equations, $\tilde{O}$ is the normalized scattered field component; E_0 is the amplitude of the incident plane wave; and $\vec{k}^{\mathrm{s}} = \vec{k}^{\mathrm{s}}(\vec{r})$ and $\vec{k}^{\mathrm{i}}$ denote the wave vectors for the observation direction and the direction of incidence. The vector $\hat{p}$ is the "polarization selection" vector, and $\mathcal{F}^{-1}$ denotes the inverse Fourier transform:

$$\tilde{O}(\vec{k}) = \mathcal{F}^{-1}\left\{O(\vec{r})\right\}(\vec{k}) = \int_{-\infty}^{\infty} O(\vec{r}')e^{j\vec{k}\cdot\vec{r}'}d^3\vec{r}'. \tag{2}$$

Dropping PO conditions or the infinite bandwidth correlates with a shape function which does not exactly represent the illuminated surface any more.

In order to simplify notations we will now consider the two-dimensional case [1, 2] (the three-dimensional case is a straightforward extension of the two-dimensional case). Equation (2) written in Cartesian coordinates reads

$$\tilde{O}(k_x, k_z) = \int_{-\infty}^{\infty}\int_{-\infty}^{\infty} O(x, z)e^{jk_x x + jk_z z}dxdz. \tag{3}$$

Consequently, the Fourier transform of the scattered field delivers the shape function (the image):

$$O(x, z) = \frac{1}{(2\pi)^2}\int_{-\infty}^{\infty}\int_{-\infty}^{\infty} \tilde{O}(k_x, k_z)e^{-jk_x x - jk_z z}dk_x dk_z \tag{4}$$

where the spectral integration is carried out over the complete $(\vec{k}^{\mathrm{s}} - \vec{k}^{\mathrm{i}})$ space.

The fast imaging algorithm to be summarized in the following has been described first for the SBR method by Bhalla & Ling. The full-wave imaging and scattering center formulation however is an extension of Bhalla & Lings technique, so it is reasonable to first summarize their SBR-based approach. The full-wave imaging extension will be described subsequently. Here and in the following we assume perfectly conducting scatterers in order to simplify notations (our SBR-based fast imaging implementation however also covers coatings and edge scattering).

The SBR formulation considered by Bhalla & Ling [3] uses electric and magnetic fields on the exit-ray cross sections as sources for the scattered field which is in contrast to our own SBR formulations

where the PO surface current density is integrated on the surface of the scatterer (over the surface-projected ray cross sections). The SBR expression for the scattered field used by Bhalla & Ling basically looks like

$$\begin{pmatrix} E_\theta^{\text{s}} \\ E_\phi^{\text{s}} \end{pmatrix} = \frac{e^{-jkr}}{r} \sum_i \begin{pmatrix} B_\theta \\ B_\phi \end{pmatrix}_i \left(\frac{jk}{2\pi} \right) (\Delta A)_i \, S_i(\theta, \phi) \, e^{j\vec{k}\cdot\vec{r}_{A_i}}. \tag{5}$$

In our formulation, $(\Delta A)_i$ are projections onto the scatterers surface. In the case of a perfectly conducting surface $B_{\theta,\phi}$ are then given as $B_{\theta,\phi} = -\eta J_{\theta,\phi}/2$ with the electric surface current density $\vec{J}$ and free space impedance η. $\vec{r}_{A_i}$ denote the hit points of the rays. The $\vec{k} = \vec{k}(\vec{r})$ in the exponential is the observation wave vector $\vec{k}^{\text{s}}(\vec{r})$. The exponential is the so-called "farfield Green's function"[†]. In order to allow for the analytical calculation of the imaging Fourier integrals, it is essential to assume that the ray patterns $S_i(\theta, \phi)$ are constant within the bistatic angular imaging area ($(\Delta A)_i$ need to be sufficiently small).

We do not repeat Bhalla & Lings derivation here in detail. A more detailed explanation can be found in the references.

Bhalla & Ling have described their algorithm for the 2-D case (see Fig. 1). The incident wave travels into $-\hat{z}$ direction, and x is the crossrange coordinate. The scattered field is evaluated for small bistatic angles $-\theta_0 \le \theta \le \theta_0$ only in order to introduce small angle approximations. Additionally a small bandwidth assumption is necessary. Both assumptions together allow to introduce the approximations $k_x \approx k_0\theta$, $k_z \approx 2k$, and $\vec{k} \cdot \vec{r}_{A_i} \approx k_0\theta x_i + kz_i$ (argument of the exponential in Equation (5)) with the two-dimensional hit point $\vec{r}_{A_i} = (x_i, 0, z_i)$ and the center frequency wavenumber k_0.
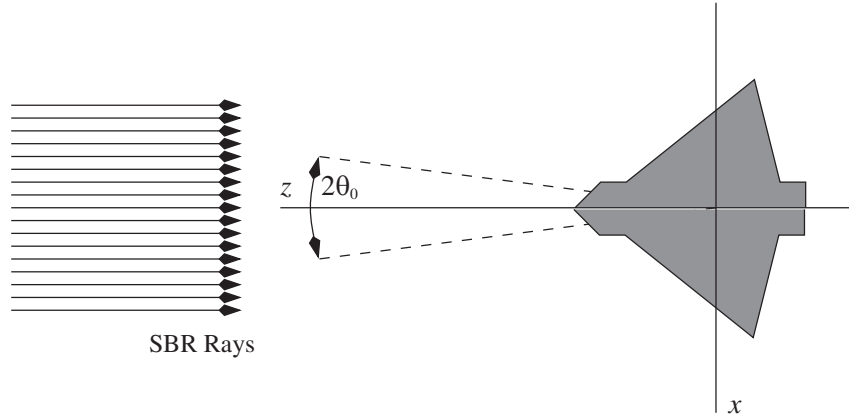
Figure 1. 2-D imaging coordinate system and definition of the maximum bistatic scan angle.

The transform from Cartesian to spherical electric field components introduces angular functions. The angular functions could be approximated by their small argument approximations, but we here deviate from Bhalla & Lings approach and image the Cartesian components of the farfield vector potentials instead[‡]. The biggest impact of this choice is seen in the 3-D case where even products of angular functions occur (see [8], for example). Another formal advantage of using the farfield vector potentials is that they do not require normalization (apart from E_0, Equations (1a) and (1b)). A disadvantage of working with the up to six Cartesian components however is that non-radiating parts are also processed and need to be represented by the scattering center model extracted from the image.

The scattered field in Equation (5) is normalized according to Equations (1a) and (1b). We then insert the normalized scattered field component (or vector potential component) into Equation (4) and switch to new integration variables k and θ. We factorize the combined exponential in Equation (4) as

$$e^{j\vec{k}\cdot\vec{r}_{A_i}} \, e^{-jk_x x - jk_z z} \approx e^{-jk(2z-z_i)} e^{-jk_0\theta(x-x_i)} \tag{6}$$

[†] For large observation point distances, $\frac{e^{-jkR}}{R} \approx \frac{e^{-jkr}}{r} \cdot e^{jk\hat{r}\cdot\vec{r}'}$ with $R = |\vec{r} - \vec{r}'|$ and $k\hat{r} = \vec{k}$ is a valid approximation. Here $\vec{r}$ denotes the observation point vector, and $r = |\vec{r}|$ and $\hat{r}$ denote its length and its direction. $\vec{r}'$ is the source point vector.

[‡] The farfield vector potentials are termed like this because they involve the farfield Green's function.

so that the first exponential on the right hand side is frequency dependent, and the second one just has an angular dependence. This will allow to factorize subsequent integrations over frequency and angle.

In the SBR, the dependence of the surface current density component on the ray length d_i is $B_i = \alpha_i e^{-jkd_i}$ with a frequency independent current coefficient α_i, altogether yielding

$$O(x,z) = -\frac{k_0}{\pi^2} \sum_i (\Delta A)_i \int_{k=k_0-\Delta k/2}^{k_0+\Delta k/2} \alpha_i e^{-jk(2z+d_i-z_i)} dk \int_{\theta=-\theta_0}^{\theta_0} e^{-jk_0\theta(x-x_i)} d\theta \tag{7}$$

with the imaging bandwidth Δk and the assumption $S_i(\theta,\phi) = 1$. For the SBR we have $\alpha_i = $ const., and analytical integration finally yields

$$O(r,x) = -\frac{2k_0\theta_0\Delta k}{\pi^2} \sum_i \alpha_i (\Delta A)_i e^{j2k_0(r-r_i)} \mathrm{sinc}\left(\Delta k(r-r_i)\right) \mathrm{sinc}(k_0\theta_0(x-x_i)) \tag{8}$$

for Equation (4). Here we have also introduced the downrange coordinate $r = -z$ and downrange positions $r_i = (d_i - z_i)/2$. This allows to introduce the two-dimensional "ray spread function" (RSF) as

$$h(r,x) = h^r(r) \cdot h^x(x) = e^{j2k_0r}\mathrm{sinc}(\Delta kr) \cdot \mathrm{sinc}(k_0\theta_0x). \tag{9}$$

The RSF could be factorized into a downrange RSF $h^r(r) = e^{j2k_0r}\mathrm{sinc}(\Delta k\, r)$ and a crossrange RSF $h^x(x) = \mathrm{sinc}(k_0\theta_0x)$. The straightforward 3-D extension involves an additional crossrange RSF $h^y(y) = \mathrm{sinc}(k_0\theta_0y)$. Furthermore, the prefactor in Equation (8) changes.

In order to derive a downrange RSF for full-wave methods, the concept developed for SBR has to be generalized. As already introduced above, in the SBR the phase of a current element B_i is related to the ray length d_i by $B_i = \alpha_i\, e^{-jkd_i}$ where α_i is a constant. We now introduce an artificial ray length d_i corresponding to the SBR first hit ray length and generalize the B_i to $B_i = \alpha_i(k)\, e^{-jkd_i}$. We essentially end up with the definition of the generalized current element specific downrange RSF:

$$h_i^r(r) = \frac{1}{\Delta k} \int_{k_0-\Delta k/2}^{k_0+\Delta k/2} \alpha_i(k)e^{j2kr}dk = e^{j2k_0r} \cdot \frac{1}{\Delta k} \int_{-\Delta k/2}^{\Delta k/2} \alpha_i(k_0+\xi)e^{j2\xi r}d\xi. \tag{10}$$

In this expression the now frequency dependent $\alpha_i(k)$ contain the "remaining" frequency dependence of the currents (apart from the "physical optics phase" related to the artificial ray length). Instead of ray hit points in SBR we now index the electric and magnetic surface current components on the Huygens surface of the full-wave methods (Huygens surface used for farfield computation, also termed "farfield contour").

The above integral is implemented as an inverse fast Fourier transform (FFT), thus reintroducing the well-known ISAR imaging frequency sampling requirement $df < c_0/(2R)$ with R denoting the target range. The element specific RSF is the main extension of the Bhalla & Ling algorithm in order to use it for full-wave field simulators.

The integral of Equation (10) is a transform from frequency domain to downrange, or equivalently, to time domain. In the case of SBR, ray lengths translate into the corresponding downrange or RSF positions $r_i = (d_i - z_i)/2$. A ray may have several hit points, and each hit point contributes with its corresponding accumulated ray length. In contrast, with the full-wave methods the "RSF position" is $r_i = -z_i$, and apart from that, contributions to the image in downrange direction are expressed solitarily by the frequency dependence of the current elements via the Fourier transform. Speaking in terms of SBR the full-wave current element may contain more than one "contribution", for example the direct contribution from the incident wave plus contributions from reflections and other scattering processes.

Concerning the SBR imaging it might be of interest that Özdemirs approach [7, p140] to image multiple hit points differs from our approach.

Another concept introduced by Bhalla & Ling is the so-called "Sullivan" scheme [2] which is used to accelerate the summation of the SBR ray contributions to the image. The direct summation would be much too costly, so an FFT-based acceleration of the convolution is a must. In the context of full-wave methods, the contributions to the image $O(r,x)$ are given by the expression (2-D)

$$O(r,x) = \sum_i \gamma_i h_i(r-r_i, x-x_i) \tag{11}$$

with the now element dependent RSF h_i instead of the standard RSF h. In the SBR case γ_i have been the current amplitude coefficients (implicitly defined by Equation (8)); now the $\alpha_i(k)$ belong to the RSF. The equation does not constitute a convolution any more, thus preventing application of the FFT. On the other hand, the RSF could still be factorized. This allows us to apply the Sullivan scheme at least for the crossrange directions, yielding a "semi-fast" algorithm.

The problem with the original Sullivan scheme is that an anterpolation onto grid points is required. It turns out that the exponential in the downrange RSF (in Equations (9) and (10)) causes large anterpolation errors because it is the term with the fastest variation (discussed in greater detail in [6] and references therein). In order to reduce anterpolation errors, we formally multiply both the RSF and the current by the exponential e^{-j2k_0r} which cancels the exponential in the RSF. As a result, the Sullivan scheme now delivers the modulated discrete image (2-D)

$$O_{\mathrm{m}}[n_r, n_x] = O[n_r, n_x]e^{-j2k_0n_r\Delta r} \tag{12}$$

with the image array indices n_r, n_x and the downrange grid discretization Δr. The additional phase term can simply be removed. The same idea is applied in [6] and references therein, but RCS computation or the necessary image re-normalization is not covered there.

Another option for the reduction of anterpolation errors is simpler but works nearly as well as the approach described above: Assigning the RSF to the nearest grid point causes a phase error for the related scattered field (due to the wrong downrange position of the RSF). Consequently a phase factor could be applied to γ_i to compensate the phase error of the monostatic scattered field at center frequency.

2.2. Scattering Center Extraction

The scattering center model can be seen as a compressed image. The RCS can be evaluated for any angle and frequency by summation over typically a few hundred scattering centers per component. The idea of the "CLEAN" algorithm proposed by Bhalla & Ling for the SBR algorithm is that the image could be expressed by just a small number of extracted RSF. The positions and amplitudes of these extracted RSF are called "scattering centers". The iterative CLEAN process searches the maximum in the image and removes the RSF weighted with the amplitude just found. The process is repeated until the image is "sufficiently clean" (max. image amplitude below -40 dB, for example).

In the case of full-wave formulations we use multiple element specific RSF, so the CLEAN algorithm does not seem applicable on first view. But in fact, it is still applicable which could be understood by seeing that a band-limited function could be expressed by sinc functions (sampling theorem). The standard RSF is a 3-D sinc function, and the image is band-limited by construction, so the CLEAN algorithm with the standard RSF should still be applicable.

For a single Cartesian component of the magnetic or electric farfield vector potentials ($\vec{\Pi}^J$, $\vec{\Pi}^M$), the scattering center model is evaluated as

$$\Pi = \frac{\pi^3}{(k_0\theta_0)^2\Delta k} \sum_n A_n \operatorname{rect}\left(\frac{k_x}{2k_0\theta_0}\right) e^{jk_xx_n} \operatorname{rect}\left(\frac{k_y}{2k_0\theta_0}\right) e^{jk_yy_n} \operatorname{rect}\left(\frac{k_z - 2k_0}{2\Delta k}\right) e^{jk_zz_n} \tag{13}$$

with the scattering center amplitudes and coordinates A_n and x_n, y_n, z_n. The wavenumbers k_x, k_y, k_z are the Cartesian components of the vector $\vec{k}^{\mathrm{s}} - \vec{k}^{\mathrm{i}}$. The rect functions formally represent the considered frequency band (k_0, Δk) and bistatic angular range (θ_0). The term $k_0\theta_0$ in the denominators is a result from the small bandwidth and small angle approximations. Nevertheless, the scattering center model is evaluated using the exact wavevectors.

The derivation of the scattering center model is done by formally transforming from image space to k-space. Essentially the standard RSF used for the cleaning need to be transformed to k-space. Furthermore, for compatibility with Equation (1b), for a balanced contribution of scattering centers to the RCS and to permit usage of the above scattering center model for both current densities (electric and magnetic) we assume that not only $\vec{\Pi}^J$ but also $\vec{\Pi}^M$ contains a factor η. As a result, magnetic surface current densities need to be scaled with $1/\eta$.

The above expression for the scattering center model is a frequency domain expression. An interesting application of the scattering center model however is to compute waveforms scattered by

an air-platform on a specific flight path. Theoretically this could be done by using Fourier transforms between time and frequency domains, but FFT application is restricted to static targets (movement with constant velocity and observation angle could be taken into account by Doppler shifting). The alternative approach uses the scattering center model directly in time domain. For the derivation of such a time domain scattering center model formulation we assume that the carrier frequency is much larger than the modulation frequency in order to simplify a time derivative (calculating the farfield from the potentials involves a time derivative). As a result, we get a very simple expression for the scattered pulse form, essentially a sum of time shifted and weighted incident waveforms (all waveforms in baseband).

3. RESULTS

3.1. Grenade Computed with DG-FEM

Figure 2 shows a grenade which is assumed to be purely metallic here. Generally we would generate multiple scattering center models for full-spherical coverage. Since each scattering center model delivers the bistatic RCS within its angular range (defined by θ_0), the "bistatic to monostatic approximation" [5] is typically used to transform the bistatic RCS into the monostatic RCS.
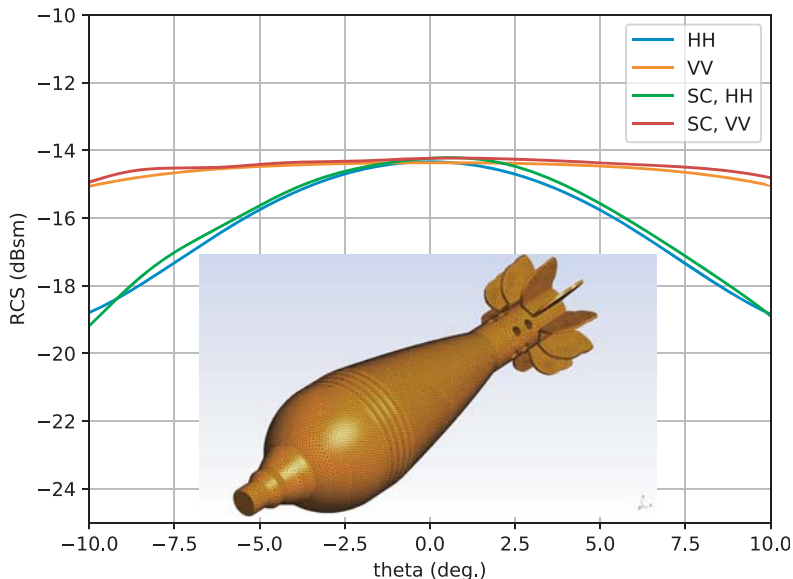
Figure 2. Angular scan of the bistatic RCS of the grenade's "nose-on cone" scattering center model at center frequency (label "SC"). Comparison with RCS directly computed by DG-FEM. The horizontal axis scan angle θ ("theta") is the bistatic angle measured from direction of incidence (see Fig. 1).

We here consider single scattering center models for a single direction of incidence only. For Fig. 2 we consider the "nose-on direction". We plot the bistatic RCS within the maximum bistatic angles $(-\theta_0 < \theta < \theta_0)$ for the center frequency. The comparison with the RCS directly computed by the DG-FEM shows a good agreement with the scattering center model derived from DG-FEM. The remaining deviations could be reduced by removing scattering centers related to noise generated by the cleaning. Another option is to apply more sophisticated cleaning algorithms. The DG-FEM used here is a GPU-accelerated multirate adaptive-order ("P-nonconformal") formulation.

Figure 3 shows a comparison of the scattering center RCS with the reference over frequency (RCS directly computed by the DG-FEM solver). The "k-space" curve is essentially the result of a Fourier transform of the image.

Concerning the imaging settings applied for all the cases shown in this section we typically use isotropic image resolution which corresponds to setting $\theta_0 = \Delta f / f_0$ with the imaging bandwidth Δf
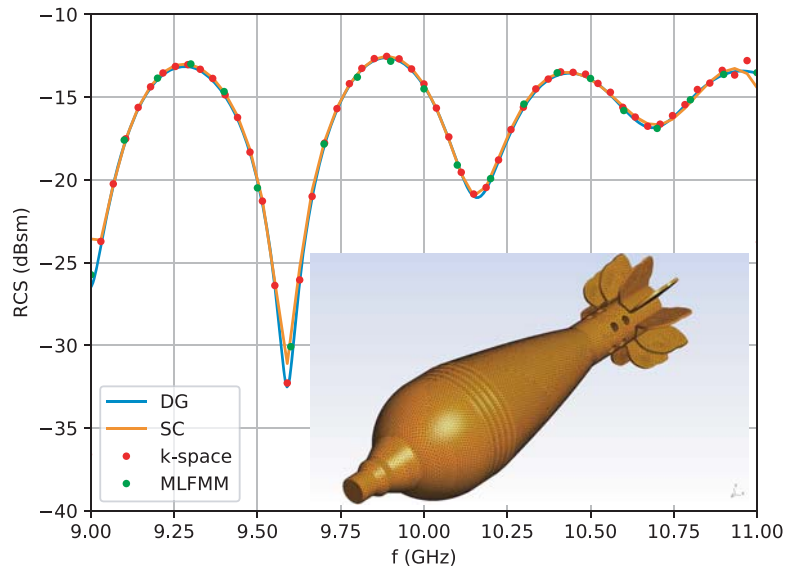
Figure 3. Frequency scan of the monostatic RCS of the grenade's "nose-on cone" scattering center model ("SC"). Comparison with RCS directly computed by DG-FEM, by MLFMM and via FFT of the image ("k-space").

and center frequency f_0. High precision "CLEAN levels" are typically between $-40\,\mathrm{dB}$ and $-50\,\mathrm{dB}$; for many practical applications, a CLEAN level of $-30\,\mathrm{dB}$ is sufficient.

3.2. Almond with Dielectric Belt Computed with DG-FEM

Figure 4 shows a scaled version of the NASA almond (for two different polarizations and imaged surface current components). Additionally we have integrated a dielectric "belt" (a thin dielectric coating,
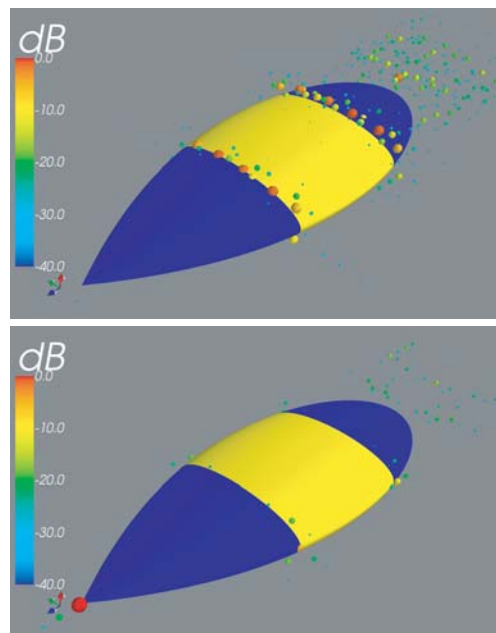
Figure 4. Scattering center models for an almond with dielectric coating (yellow). Top: Vertically (x-) polarized incident field, J_z current component. Bottom: Horizontally (y-) polarized incident field, M_x current component.

$\epsilon_{\mathrm{r}} = 16.1$, conductivity $\sigma = 6.175 \,\mathrm{S/m}$). The scattering center models are again for the nose-on direction. The top figure shows the model for the J_z component. It could be observed that the transitions between PEC and dielectric belt cause reflections (but they do not necessarily radiate). The bottom figure shows the scattering center model for the M_x magnetic surface current component. It could be observed that tip scattering occurs. The small scattering centers "behind" the target are related to "higher order effects", as they are termed in the context of SBR. In the SBR, rays seeing more than one reflection would contribute to scattering centers behind the target, translating into the corresponding phases or time delays.

Here another disadvantage of processing the surface current components instead of the fields becomes obvious: Interpretation of the up to six scattering center models might be less intuitive.

In order to investigate the precision of the scattering center model, Fig. 5 compares the scattering center RCS with the RCS directly computed by the DG-FEM and with the k-space RCS.
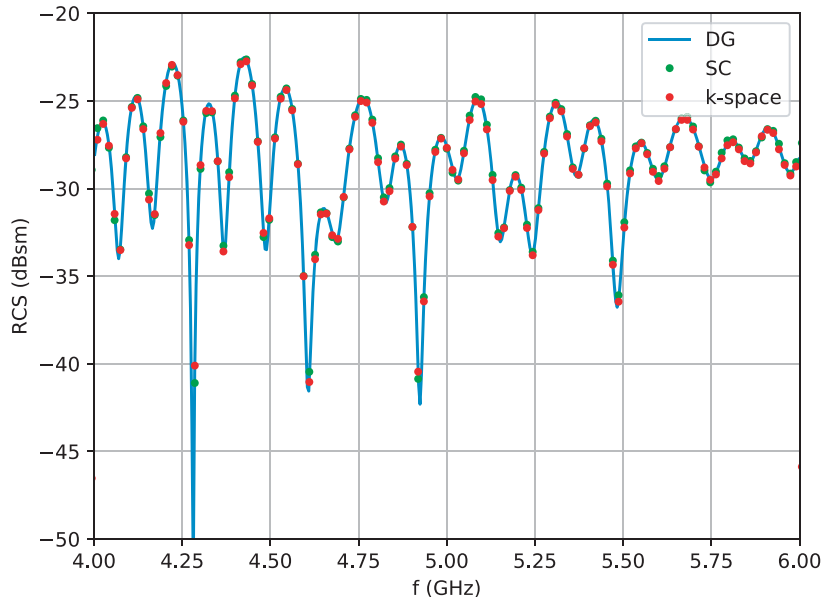
Figure 5. Frequency scan of the monostatic RCS of the almond's "nose-on cone" scattering center model ("SC"). Comparison with RCS directly computed by DG-FEM and via FFT of the image ("k-space").

At this point one may also ask how full-wave images would compare to SBR images. A prerequisite for such a comparison is that the full-wave method uses the surface of the scatterer as the farfield contour, like the SBR does it implicitly. The DG-FEM in contrast may also use other farfield contours so that both the electric and magnetic surface current densities need to be imaged. Now if the SBR is applicable, one should expect a more or less good agreement of the SBR scattering center model with the MLFMM scattering center model because the SBR inherently uses induced surface current densities for scattered field computation, like the MLFMM does.

3.3. Generic Re-Entry Vehicle Computed with MLFMM

Figure 6 shows a generic re-entry vehicle and the monostatic RCS of its "nose-on" scattering center model over frequency. In contrast to the simulations shown above, we here use the MLFMM to generate the scattering center model. The disadvantage of MLFMM is that it is costly to generate broadband information (in contrast to the time domain solvers DG-FEM or FDTD). Nevertheless, MLFMM could be advantageous if low frequency problems are considered, and individual element currents could also be interpolated over frequency to improve efficiency. Center frequency (850 MHz) and considered bandwidth (170 MHz) are quite small for imaging purposes, but the scattering center model is seen to be valid.
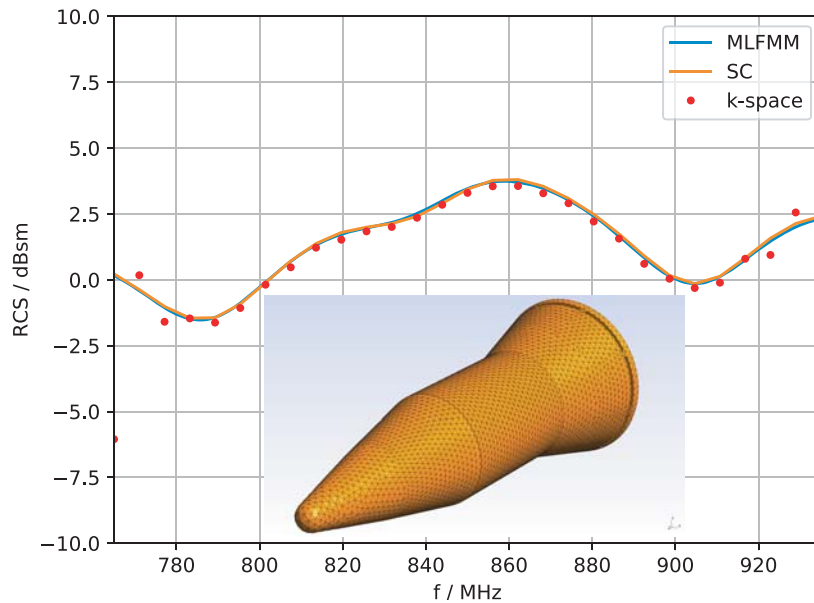
Figure 6. Frequency scan of the monostatic RCS of a generic re-entry vehicle's "nose-on cone" scattering center model ("SC"). Comparison with RCS directly computed by MLFMM and via FFT of the image ("*k*-space").

4. CONCLUSION

We have introduced an extension of the SBR-based imaging and scattering centers algorithm originally proposed by Bhalla & Ling in order to render it applicable to full-wave methods. Due to the "phase extraction" discussed above (Section 2.1) the computational resources required for the imaging and scattering center extraction approach are well below the requirements for the underlying full-wave field simulator (DG-FEM, MLFMM, FDTD). In the case of SBR it is the CLEAN step which dominates the CPU time over the ray tracing (at least in the case of high precision cleaning). This step could easily be accelerated by GPU computing.

The advantage of the described fast algorithm over the traditional imaging algorithm based on RCS sampling is mainly related to the relaxed angular sampling requirement. The angular sampling in the fast algorithm (distribution of the bistatic cones for full-spherical coverage) is essentially determined by the bistatic to monostatic approximation since the Bhalla & Ling formulation itself allows to use quite large bistatic angles. In the case of SBR an additional advantage of the fast algorithm is that the frequency loop is eliminated.

In any case, the RCS of a target is most efficiently stored in the form of a scattering center model. Furthermore, the scattering center model allows to extract the RCS for "arbitrary" observation angles and frequencies by summing over a few hundred scattering centers per component.

REFERENCES

1. Bhalla, R. and H. Ling, "ISAR image formation using bistatic data computed from the shooting and bouncing ray technique," *Journal of Electromagnetic Waves and Applications*, Vol. 7, No. 9, 1271–1287, Jan. 1993.

2. Bhalla, R. and H. Ling, "A fast algorithm for signature prediction and image formation using shooting and bouncing rays technique," Tech. Rep., Department of Electrical and Computer Engineering, The University of Texas at Austin, Austin, TX 78712-1084, Jan. 1994.

3. Bhalla, R. and H. Ling, "Image-domain ray-tube integration formula for the shooting and bouncing ray technique," Tech. Rep., Department of Electrical and Computer Engineering, The University of Texas at Austin, Austin, TX 78712-1084, Jul. 1993.

4. Bhalla, R. and H. Ling, "Three-dimensional scattering center extraction using the shooting and bouncing ray technique," *IEEE Trans. Antennas Propagat.*, Vol. 44, No. 11, 1445–1453, Nov. 1996.

5. Schuh, M., A. Woo, and M. Simon, "The monostatic/bistatic approximation," *IEEE Antennas Propag. Mag.*, Vol. 36, No. 4, 76–78, Aug. 1994.

6. Yun, D.-J., J.-I. Lee, K.-U. Bae, J.-H. Yoo, K.-I.'Kwon, and N.-H. Myung, "Improvement in computation time of 3-d scattering center extraction using the shooting and bouncing ray technique," *IEEE Trans. Antennas Propagat.*, Vol. 65, No. 8, 4191–4199, Aug. 2017.

7. Özdemir, C., *Inverse Synthetic Aperture Radar Imaging with MATLAB Algorithms*, John Wiley & Sons, Inc., Feb. 2012.

8. Buddendick, H. and T. F. Eibert, "Bistatic image formation from shooting and bouncing rays simulated current distributions," *Progress In Electromagnetics Research*, Vol. 119, 1–18, 2011.